

Article

# The Effect of Packing Material Properties on Tars Removal by Plasma Catalysis

Richard Cimerman <sup>1,\*</sup> , Mária Cíbiková <sup>1</sup>, Leonid Satrapinsky <sup>2</sup> and Karol Hensel <sup>1</sup> 

<sup>1</sup> Department of Astronomy, Physics of the Earth and Meteorology, Faculty of Mathematics, Physics and Informatics, Comenius University, Mlynská Dolina F2, 842 48 Bratislava, Slovakia; cibikova17@uniba.sk (M.C.); karol.hensel@fmph.uniba.sk (K.H.)

<sup>2</sup> Department of Experimental Physics, Faculty of Mathematics, Physics and Informatics, Comenius University, Mlynská Dolina F2, 842 48 Bratislava, Slovakia; leonid.satrapinsky@fmph.uniba.sk

\* Correspondence: richard.cimerman@fmph.uniba.sk

Received: 15 November 2020; Accepted: 14 December 2020; Published: 17 December 2020



**Abstract:** Plasma catalysis has been utilized in many environmental applications for removal of various hydrocarbons including tars. The aim of this work was to study the tars removal process by atmospheric pressure DBD non-thermal plasma generated in combination with packing materials of various composition and catalytic activity ( $\text{TiO}_2$ ,  $\text{Pt}/\gamma\text{Al}_2\text{O}_3$ ,  $\text{BaTiO}_3$ ,  $\gamma\text{Al}_2\text{O}_3$ ,  $\text{ZrO}_2$ , glass beads), dielectric constant (5–4000), shape (spherical and cylindrical pellets and beads), size (3–5 mm in diameter, 3–8 mm in length), and specific surface area (37–150  $\text{m}^2/\text{g}$ ). Naphthalene was chosen as a model tar compound. The experiments were performed at a temperature of 100 °C and a naphthalene initial concentration of approx. 3000 ppm, i.e., under conditions that are usually less favorable to achieve high removal efficiencies. For a given specific input energy of 320 J/L, naphthalene removal efficiency followed a sequence:  $\text{TiO}_2 > \text{Pt}/\gamma\text{Al}_2\text{O}_3 > \text{ZrO}_2 > \gamma\text{Al}_2\text{O}_3 > \text{glass beads} > \text{BaTiO}_3 > \text{plasma only}$ . The efficiency increased with the increasing specific surface area of a given packing material, while its shape and size were also found to be important. By-products of naphthalene decomposition were analyzed by means of FTIR spectrometry and surface of packing materials by SEM analysis.

**Keywords:** non-thermal plasma; dielectric barrier discharge; plasma catalysis; naphthalene removal; FTIR spectrometry; SEM analysis;  $\text{TiO}_2$ ;  $\text{Pt}/\gamma\text{Al}_2\text{O}_3$ ;  $\text{ZrO}_2$ ;  $\text{BaTiO}_3$

## 1. Introduction

In recent years, non-thermal plasma (NTP) generated by atmospheric pressure electric discharges in a combination with catalysis, i.e., plasma catalysis, is gaining an increasing interest as it offers a high plasma reactivity along with a high catalytic selectivity [1,2]. In addition, plasma catalysis is often characterized by synergistic effects, when the combined effect of plasma with catalysis is usually stronger than their individual effects [3–5]. Although the exact underlying mechanisms of plasma catalysis synergy are still unclear, several hypotheses based on experimental observations have been proposed: plasma-induced adsorption/desorption, activation of lattice oxygen, lowering the activation barriers, generation of electron–hole pairs by the absorption of UV radiation, direct interaction of gaseous radicals with the catalyst surface and the adsorbed molecules, penetration of plasma reactive species into the pores of the catalyst, local heating (hot spots), etc. [2,4,6,7]. The synergy may lead to higher conversion of reactants, higher selectivity and yield of desired products as well as higher energy efficiency of the process [8,9]. Thanks to this, plasma catalysis has found utilization in many environmental applications particularly in air pollution control technologies, including removal of nitrogen oxides ( $\text{NO}_x$ ) [10–13], volatile organic compounds (VOCs) [14–17], polycyclic aromatic hydrocarbons (PAHs) [18], and conversion of carbon dioxide  $\text{CO}_2$  [8,19,20].

The utilization of NTP in the PAH removal process has been investigated by many authors and extensive and comprehensive reviews about the topic have been published in several papers [18,21–23]. Although the PAH removal by plasma catalysis was investigated much less frequently in the past, it has gained an increasing interest in the recent years. One of the many reasons is the increasing utilization of the syngas as a possible candidate for a new environmentally friendly source of energy [24]. The syngas, as a product of a gasification of carbon containing fuels including biomass, can be used to generate electricity by internal combustion gas turbines or engines, or can be transformed into chemicals. However, the syngas often contains various pollutants, especially stable PAHs–tars, that substantially disqualify it from further use [25]. Therefore, the syngas cleaning before its utilization is required. Besides gasification processes, the tars can also form in combustion processes of fossil fuels, although with lower amounts compared to gasification. However, their removal from exhaust gases is also important due to associated environmental issues [26].

Even though many published papers denoted as “plasma catalytic removal of model tar compound” can be found in the available literature, a majority of these papers actually deals with a removal of toluene ( $C_7H_8$ ) as a model tar compound [27–32]. Nevertheless, the toluene represents “only” a monocyclic organic compound as it contains a single benzene ring. The real tars formed in the gasification and combustion processes are much more complex and usually consist of several benzene rings. Further, the stability of toluene is lower and its reactivity higher in comparison with e.g., naphthalene ( $C_{10}H_8$ ), the simplest PAH containing two benzene rings. Indeed, toluene can be decomposed much more easily than naphthalene as a consequence of weaker C–C bonds in a toluene molecule due to the presence of methyl group— $CH_3$  [33]. Furthermore, decomposition of polycyclic tars with three or more benzene rings may lead to a formation of two-ring tars, just like naphthalene, that are often more stable than heavier polycyclic compounds [34]. For these reasons, a better candidate representing a group of tars is naphthalene rather than toluene.

A recent review paper written by Liu et al. focused on plasma catalytic removal of tars offers a very good overview of the field [18]. It summarizes the general knowledge, recent experiments, results, and findings of various authors. Indeed, several discharges have been employed and investigated in the naphthalene removal process by plasma catalysis: corona discharge [35,36], dielectric barrier discharge (DBD) [37–43], gliding arc discharge [44,45], and even plasma jet [46]. The discharges have been combined with several catalytic materials, most frequently with Ni-based catalysts (Ni/ $\gamma$ - $Al_2O_3$  [37,38,40,44], Ni/ZSM-5, Ni/ $SiO_2$  [41] and Ni/Co-based catalyst [45]) due to their availability and selectivity towards formation of syngas constituents in catalytic processes [23]. However, their high activities are obtained only when operated at elevated temperatures ( $>780$  °C) [47]. Besides Ni-based catalysts, other materials have also been investigated in a plasma catalytic process of naphthalene removal, including  $MnO_2$  [35],  $\gamma$ - $Al_2O_3$  [36], Rh- $LaCoO_3/Al_2O_3$  [40],  $TiO_2$ /diatomite [43], and Pt/ $\gamma$ - $Al_2O_3$  [46].

The main objective of this work is to investigate tar removal by atmospheric pressure DBDs in combination with packing materials of various properties and catalytic activities. Naphthalene is selected as a model tar compound. The research follows our previous work [48], where naphthalene removal was investigated using  $TiO_2$ , Pt/ $\gamma$ - $Al_2O_3$ ,  $\gamma$ - $Al_2O_3$  and glass beads as packing materials. Here, we also study the effect of other materials including  $ZrO_2$  and  $BaTiO_3$ . The used packing materials are characterized by distinct shape (spherical and cylindrical pellets and beads), size (3–5 mm in diameter, 3–8 mm in length), dielectric constant (5–4000), and specific surface area (SSA) (37–150  $m^2/g$ ). In comparison with the existing works of other authors, this work presents a comparative study on several packing materials of various properties and reports their plasma catalytic effects in naphthalene removal. The experiments are performed at a temperature of approx. 100 °C and a naphthalene initial concentration of approx. 3000 ppm, i.e., under conditions that are usually less favorable to achieve high removal efficiencies. Besides the effects of packing material properties on naphthalene removal efficiency, a formation of by-products of naphthalene decomposition is also studied. The by-products

are analyzed by means of Fourier-transform infrared (FTIR) spectrometry and surface of packing materials by scanning electron microscope (SEM) analysis.

## 2. Results and Discussion

### 2.1. Discharge Characteristics

Prior to the experiments on naphthalene removal, we evaluated the discharge power of all DBD reactors by using the Lissajous figure method. The results showed that, at a given applied voltage, the reactors packed with Pt/ $\gamma$ -Al<sub>2</sub>O<sub>3</sub>,  $\gamma$ -Al<sub>2</sub>O<sub>3</sub>, ZrO<sub>2</sub>, TiO<sub>2</sub> (SSA of 70 m<sup>2</sup>/g) and glass beads ( $\varnothing$  4 mm) had almost the same discharge power, whereas the power of plasma non-packed reactor as well as the reactor packed with BaTiO<sub>3</sub> significantly differed (see Figure 1a,b, where discharge power is expressed in terms of the specific input energy (SIE)). Note that uncertainty of the data points in Figure 1a,b is approx. 5–6%. Indeed, at the given applied voltage, the SIE of the plasma non-packed reactor was always higher than that of packed reactors (Figure 1a). On the contrary, the reactor packed with BaTiO<sub>3</sub> possessed the lowest discharge power in a range of the applied voltage of 11–14 kV (Figure 1a). Thus, a presence of the packing material inside the reactor generally decreases the discharge power under the same operating conditions. These findings are in agreement with the results of other authors, who also observed the same effect [49–51]. Inserting the packing material into a discharge gap has an influence on discharge mode [52,53], when the filamentary discharge mode typical for non-packed DBD reactors may change into surface discharge mode or into their combination [54]. Such change in discharge mode can also occur with the increasing of the applied voltage [55]. Furthermore, each pellet of packing material functions as a capacitor, so the charges can be trapped rather than being transferred across the gap, which also may affect the discharge current and its mode [49]. Thus, all these effects have an impact on the discharge properties including power consumption.

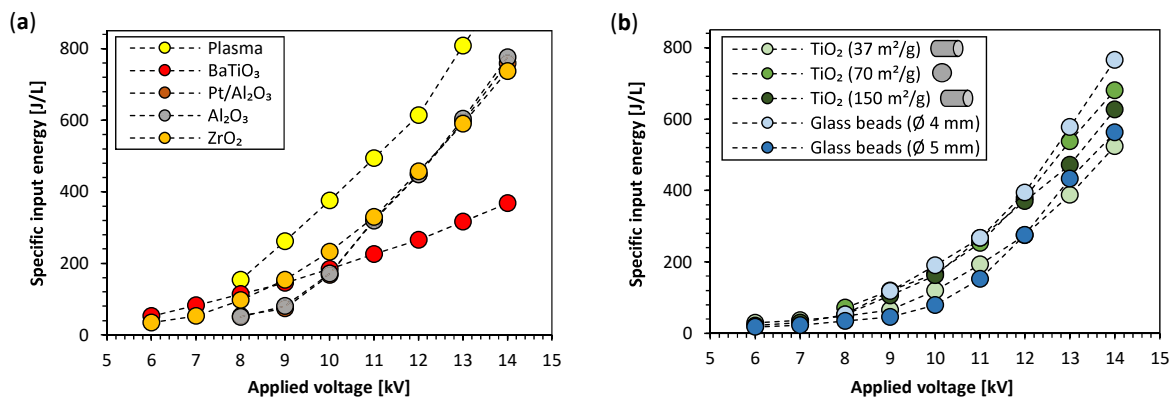


Figure 1. (a,b) Specific input energy as a function of applied voltage for various reactors (at 500 Hz).

In addition to the type of packing material, we also investigated the effects of its other properties (i.e., shape, size, SSA) on the discharge power. Packing materials of the two basic shapes were used. While packing materials including BaTiO<sub>3</sub>, Pt/ $\gamma$ -Al<sub>2</sub>O<sub>3</sub>,  $\gamma$ -Al<sub>2</sub>O<sub>3</sub>, TiO<sub>2</sub> (SSA of 70 m<sup>2</sup>/g) and glass beads possess a spherical shape, ZrO<sub>2</sub> had a cylindrical pellet shape. However, a different shape of ZrO<sub>2</sub> in comparison with the other packing materials did not show any effect on discharge power (Figure 1a).

The effect of the SSA of packing material was also investigated in a case study of TiO<sub>2</sub>. Three different SSAs were examined: TiO<sub>2</sub> with SSA of 70 m<sup>2</sup>/g had a spherical shape ( $\varnothing$  3–4 mm), TiO<sub>2</sub> with SSA of 37 and 150 m<sup>2</sup>/g had a cylindrical shape ( $\varnothing$  3–4 mm, length up to 7 mm). All parameters are indicated in the legend of Figure 1b for a clarity. When comparing TiO<sub>2</sub> with SSA of 37 and 150 m<sup>2</sup>/g, the discharge power was found to be higher for TiO<sub>2</sub> with bigger SSA (Figure 1b). It can be explained by the fact that, besides discharges propagating in gas volume and on surfaces on the packing material, a plasma may be also formed inside the pores of packing material [56–58]. In such case, bigger SSA means higher pore volume

and higher volume of generated plasma and, thus, higher discharge power. Nevertheless, at the highest amplitudes of the applied voltage (13 and 14 kV), spherical  $\text{TiO}_2$  with moderate SSA of  $70 \text{ m}^2/\text{g}$  reached even higher discharge power than  $\text{TiO}_2$  with bigger SSA of  $150 \text{ m}^2/\text{g}$  (Figure 1b). This result indicates that, at the highest tested amplitudes of the applied voltage, the effect of shape of packing material probably tends to dominate over the effect of SSA on discharge power.

Finally, the effect of size of packing material on discharge power was examined and also found to be significant. A discharge power of reactor packed with smaller glass beads ( $\text{Ø} 4 \text{ mm}$ ) was found to be higher than that of a reactor packed with larger glass beads ( $\text{Ø} 5 \text{ mm}$ ) (Figure 1b). It can be possibly explained by the fact that, when smaller beads are used in the same vessel, their total surface area is bigger, what can enhance a propagation of surface discharges in contrast to larger beads, where a shift from a full gap discharge to localized microdischarges occurs [52]. Thus, with smaller beads, the number of surface discharges and total volume of generated plasma is bigger, what leads to a higher discharge power. Another explanation of higher discharge power obtained with smaller beads is electric field enhancement in their contact points. Van Laer and Bogaerts reported a stronger electric field with smaller beads in contrast to bigger ones, what could eventually also lead to higher discharge power [52].

## 2.2. The Effect of Packing Material Type

Figure 2a,b presents naphthalene removal efficiency (NRE) and energy efficiency (EE) obtained with various plasma (non-packed) and plasma catalytic (packed) reactors. While the results obtained with  $\text{TiO}_2$ ,  $\text{Pt}/\gamma\text{Al}_2\text{O}_3$ ,  $\gamma\text{Al}_2\text{O}_3$ , and glass beads were reported in our previous paper [48], the results obtained with  $\text{BaTiO}_3$  and  $\text{ZrO}_2$  are new and presented along with our previous results. Note that each experiment was usually performed 2–5 times. Data presented in Figure 2a,b (and also in Figure 3a,b) represent mean values of NRE and EE evaluated from all experiments. The error bars represent standard deviations of the data. In addition to plasma catalytic experiments, the effect of packing material alone (i.e., without a plasma) was also tested; however, no notable effect was observed on naphthalene decomposition and gaseous products formation.

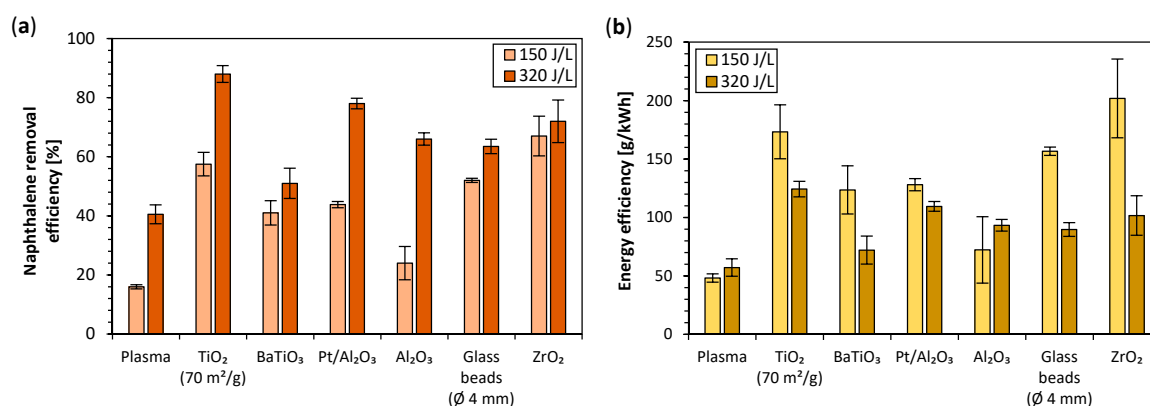


**Figure 2.** (a) Naphthalene removal efficiency and (b) energy efficiency for plasma and plasma catalytic reactors with various packing materials for the SIE of 150 and 320 J/L.

For the given SIE of 320 J/L, the NRE and the EE of all reactors followed a sequence:  $\text{TiO}_2 > \text{Pt}/\gamma\text{Al}_2\text{O}_3 > \text{ZrO}_2 > \gamma\text{Al}_2\text{O}_3 > \text{glass beads} > \text{BaTiO}_3 > \text{plasma only}$  (Figure 2a,b). Thus, the highest NRE of approx. 88% for the SIE of 320 J/L was reached with plasma catalytic reactor packed with titanium dioxide  $\text{TiO}_2$  (also called as titania) with a spherical pellet shape and SSA of  $70 \text{ m}^2/\text{g}$ . Furthermore, not only the highest NRE, but also the highest EE of 124 g/kWh was reached (for 320 J/L). High activity of  $\text{TiO}_2$  in plasma catalytic removal of naphthalene was also reported by Wu et al. [43], who obtained a similar NRE of 88%, however, at lower naphthalene initial concentration of 60 ppm. High NRE may be probably attributed to its photocatalytic activity initiated by the absorption of UV radiation emitted by

plasma [59,60] or, more likely, by interaction with plasma-produced highly energetic electrons [8,61,62]. When a reactor packed with TiO<sub>2</sub> without a plasma was tested, no effect on naphthalene decomposition was observed probably due to the absence of UV radiation and energetic electrons that are crucial for its activation [63].

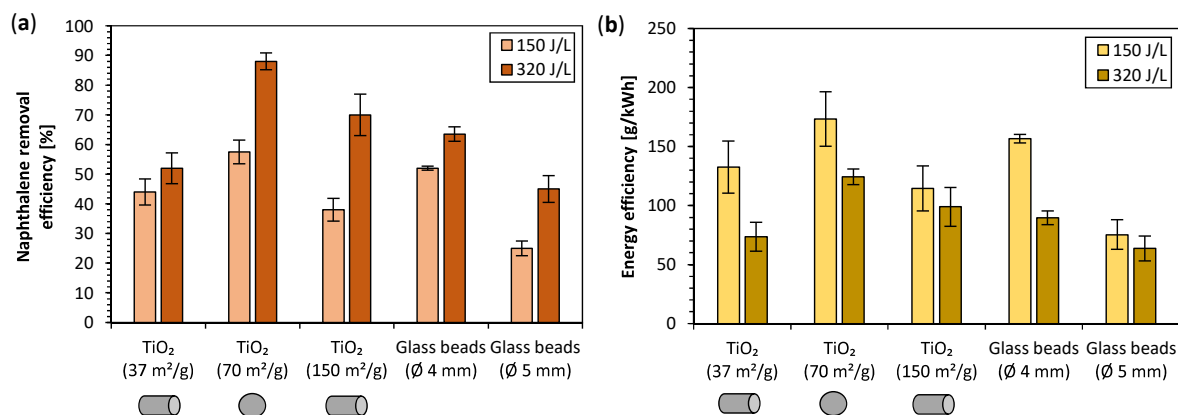


**Figure 3.** (a) Naphthalene removal efficiency and (b) energy efficiency for plasma catalytic reactors packed with TiO<sub>2</sub> of various SSAs and shapes and with glass beads of various diameters for the same SIE of 320 J/L.

The second highest NRE and EE of 78% and 110 g/kWh for the SIE of 320 J/L was obtained with a Pt/ $\gamma$ -Al<sub>2</sub>O<sub>3</sub> catalyst (Figure 2a,b). A discussion related to the results obtained with Pt/ $\gamma$ -Al<sub>2</sub>O<sub>3</sub> can be found in our previous paper [48]. The Pt/ $\gamma$ -Al<sub>2</sub>O<sub>3</sub> catalyst was also tested by Yuan et al. in combination with radio-frequency-powered plasma jet in ambient air assisted by Ar mixture for naphthalene and n-butanol removal [46]. The authors reported a superior increase of the NRE when a catalyst was used (approx. 99%) compared to a reactor without it (30%). Various other Pt-based catalysts have also been extensively investigated on catalytic naphthalene removal and their high activity was commonly reported [64–66]. In addition to high catalytic activity, high CO<sub>2</sub> selectivity was also observed [64,67]. These works showed that Pt-based catalysts are efficient not only for catalytic VOC removal as is generally well-known [68,69], but are also very active for catalytic decomposition of more complex molecules including PAHs. However, Ndifor et al. and Shie et al. reported catalytic activity of Pt/ $\gamma$ -Al<sub>2</sub>O<sub>3</sub> towards naphthalene oxidation only above 150 °C [64,65], i.e., at temperatures higher than in our experiment. Our results showed that Pt/ $\gamma$ -Al<sub>2</sub>O<sub>3</sub> may also be efficient at a lower temperature of 100 °C, but only when plasma catalysis is employed.

Another tested metal oxide catalyst was zirconium dioxide ZrO<sub>2</sub> (zirconia). Although for 320 J/L the zirconia reached the third highest NRE, for lower SIE of 150 J/L, it reached the highest NRE and EE among all tested packing materials of approx. 67% and 202 g/kWh, respectively. The zirconia is widely used as a catalyst support, but it also provides an intrinsic catalytic activity [70,71]. Moreover, a very promising catalytic activity of zirconia for high-temperature oxidation of tars was observed by several authors [72–74]. According to our results, we suppose that the zirconia, like Pt/ $\gamma$ -Al<sub>2</sub>O<sub>3</sub>, may manifest a high catalytic activity even at lower temperatures when activated by plasma. Another reason for a relatively high NRE obtained with zirconia can be, like titania, associated with its photocatalytic activity, although its band gap is much wider (5.5–7 eV), than that of titania (3–3.2 eV) [75,76]. As the intensity of the UV radiation generated by air atmospheric pressure discharges necessary for zirconia photocatalytic activation (e.g., below 225 nm) is typically very low [77], we assume that the catalyst activation can only be initiated by plasma-produced highly energetic electrons [8,61,62].

The NRE obtained with  $\gamma$ -Al<sub>2</sub>O<sub>3</sub> (alumina) and glass beads were almost identical: 66 and 64% for the SIE of 320 J/L. More details can be found in [48]. Plasma catalytic removal of naphthalene by using pulsed corona discharge combined with  $\gamma$ -Al<sub>2</sub>O<sub>3</sub> was also investigated by Nair [36]. He reported an increase of the NRE (>95%) and a reduction of energy demand when plasma catalysis was employed in

contrast to the case of plasma alone. He worked at a temperature of 300 °C and at an initial naphthalene concentration of 500–700 ppm. Although  $\gamma\text{Al}_2\text{O}_3$  is the most commonly used bulk material for the supported catalysts, its properties may also play an important role in enhancing the catalytic performance of supported catalysts [78,79]. In addition,  $\gamma\text{Al}_2\text{O}_3$  has an ability to adsorb organic compounds [80], which may increase the overall efficiency of their removal and even to enhance CO oxidation [81]. Moreover, Roland et al. suggested that  $\gamma\text{Al}_2\text{O}_3$  is able to enhance a decomposition of ozone  $\text{O}_3$  leading to a formation of O radicals, what in turn may enhance plasma catalytic VOC oxidation [82]. This effect was also proposed by Wu et al. for observed improvement in naphthalene removal over  $\text{TiO}_2$ /diatomite catalyst, as the diatomite is composed of approx. 16% of  $\gamma\text{Al}_2\text{O}_3$  [43]. With regard to the effect of glass beads as a packing material, their utilization in naphthalene removal was also studied by Hübner et al. [39] and Redolfi et al. [42]. They obtained an NRE of 60 and 95%, however, at higher operating temperatures of 350 and 250 °C and at significantly lower naphthalene initial concentrations of 90 and 100 ppm, respectively. Even though the glass beads represent a dielectric material without any specific catalytic activity, their role in improvement of the NRE probably lies in affecting the discharge characteristics, quality, and distribution [83].

Finally, the reactor packed with  $\text{BaTiO}_3$ , a high dielectric constant material (~4000), was also tested. A purpose for introducing of ferroelectric packing materials in a plasma reactor is generally to amplify the electric field. Because of this, a distribution of electrons is shifted towards higher energies and, thus, a generation of high-energy species in the discharge zone is established [84]. Although inserting the  $\text{BaTiO}_3$  resulted in a significant change of characteristics of discharge current pulses (not showed), the chemical effects of  $\text{BaTiO}_3$  reactor were found to be relatively weak. The NRE obtained with  $\text{BaTiO}_3$  was the lowest among all plasma catalytic packed reactors: for the SIE of 320 J/L, the NRE and EE were 51% and 72 g/kWh, respectively (Figure 2a,b). The high dielectric constant packing materials constrain a discharge distribution predominantly to the contact points of the pellets, regardless of their contribution to electric field enhancement [53]. The discharge exhibits a filamentary microdischarge mode without surface discharges propagating along the packing material. This limits a catalyst surface area exposed to plasma resulting in a low catalytic activity. Dielectric constant of the other packing materials tested in our study is considerably lower (glass beads~5,  $\gamma\text{Al}_2\text{O}_3$ ~9,  $\text{ZrO}_2$ ~20,  $\text{TiO}_2$ ~85,  $\text{Pt}/\gamma\text{Al}_2\text{O}_3$ ~100), what is in favor of the formation of surface discharges in these reactors (indirect evidence of their presence is presented in Section 2.4.1). Based on our results, we can conclude that a key factor for obtaining a substantial NRE is a presence of surface discharges propagating along the packing material. Firstly, they distribute a plasma more uniformly and intensively within a reactor and, secondly, they activate a larger area of the catalyst. The importance of surface discharges for attaining good catalytic activity in plasma catalysis was also confirmed by Kim et al. [85] and Veerapandian et al. [16]. On the other hand, high dielectric constant materials may find a possible utilization in applications where high-energy electrons are required in order to obtain good efficiencies (i.e., conversion of  $\text{CO}_2$ ) [19,86,87].

### 2.3. The Effect of Packing Material Properties (SSA, Shape, and Size)

The effect of packing material properties (SSA, shape, and size) on NRE and EE was also studied and evaluated. Although the effect of SSA on plasma physical characteristics as well as SIE was relatively small (Figure 1b), it was expected to have much stronger impact on chemical processes on the surface of the packing material. An increase of the SSA leads to enhancement of adsorption of target compounds on the material surface that may further support their oxidation and formation of by-products [16]. This effect was also observed for naphthalene when it was adsorbed on materials of various SSAs [88,89]. Adsorption of target compounds may also be influenced by other textural properties of packing materials (e.g., pore size and volume). Furthermore, plasma reactive species can diffuse into catalyst pores, which may lead to an enhanced catalytic activity [57]. On the other hand, a variation of shape and size of packing materials may alter and enhance the electric field, and consequently plasma properties. Plasma formation and distribution inside the packed reactor

may be affected as well, what can also eventually lead to enhanced chemical effects under plasma catalysis [16,52,86].

In the previous Section 2.2., we presented the results of the effects of various types of packing materials on the NRE. A presented sequence of the used materials ordered with respect to the achieved NRE is valid, although the effect of SSA was not explicitly considered despite it possibly affects the overall results. The SSA of a material is one of the most critical parameters for conventional catalysis. In order to accurately assess the effects of various types of packing materials, they should possess a similar SSA. Although the SSA of the used packing materials was not always known, our results showed that the role of SSA in plasma catalysis is not decisive as it is in conventional catalysis. More specifically,  $\gamma\text{Al}_2\text{O}_3$  and glass beads are characterized by very distinct SSAs (typically 250–300  $\text{m}^2/\text{g}$  [85] and  $<0.001 \text{ m}^2/\text{g}$ , respectively). Despite the huge difference in the SSA of the two materials, our results indicate that for the same SIE of 320 J/L, the NRE for  $\gamma\text{Al}_2\text{O}_3$  and glass beads is almost the same (66% and 64%, respectively). Therefore, we suppose that, in plasma catalysis, in addition to SSA, other parameters may play more important roles. Nevertheless, in this study, the effect of SSA along with the effect of shape of packing material was investigated in a case study of  $\text{TiO}_2$ .

Figure 3a,b presents the NRE and EE for reactors packed with  $\text{TiO}_2$  catalysts of various SSAs and shapes and glass beads of various sizes. With an increase of SSA (37 vs. 150  $\text{m}^2/\text{g}$ ), we observed an increase of NRE and EE for the same SIE (52 vs. 70% and 74 vs. 99 g/kWh for 320 J/L, respectively). It can be probably explained by enhanced adsorption processes on the catalyst surface and, thus, more efficient naphthalene decomposition. A change of packing material shape (spherical vs. cylindrical) was found to have an even stronger effect than a change in the SSA with respect to NRE and EE, as a spherical  $\text{TiO}_2$  catalyst of 70  $\text{m}^2/\text{g}$  showed higher NRE and EE (88% and 124 g/kWh for 320 J/L, respectively) than cylindrical  $\text{TiO}_2$  with a bigger SSA of 150  $\text{m}^2/\text{g}$  (70% and 99 g/kWh for 320 J/L, respectively). This result can be explained by the fact that the shape of the packing material determines the size of voids/spaces between the pellets, and thus discharge properties and plasma volume (this effect is also discussed later in Section 2.4.1). The result also demonstrates one of the main differences between plasma catalysis and conventional catalysis, in which SSA (or textural properties of packing materials in general) plays a crucial and often a decisive role. In plasma catalysis, not only textural properties of packing materials, but also properties of plasma as well as complex interactions between them determine the overall effect.

Finally, our results also revealed a positive effect of smaller glass beads ( $\text{Ø}$  4 mm) when compared to larger glass beads ( $\text{Ø}$  5 mm), as the NRE and EE were higher with smaller beads for both tested SIE values (for 320 J/L, 64 vs. 45% and 90 vs. 64 g/kWh, respectively). It can possibly be explained by a bigger total surface area of smaller beads that consequently leads to an enhancement of surface discharges propagation along the surface of beads. In the case of larger beads, a shift from full gap discharge to localized microdischarges occurs [52]. For this reason, an enhancement in surface discharges, as we stated earlier, could finally lead to higher removal efficiency. However, Van Laer and Bogaerts as well as Butterworth et al. observed more complicated relationship between removal and energy efficiencies and packing material size, especially when the size of packing material becomes very small [86,90,91]. Van Laer and Bogaerts reported higher removal and energy efficiency with a packing material of diameter bigger than 1.5 mm, than for a non-packed reactor (for the discharge power of 60 W). However, when using packing of diameter smaller than 1.5 mm, removal and energy efficiency were lower than for a non-packed reactor probably due to very short gas residence time in a reactor [90,91]. Furthermore, Butterworth et al. reported that the use of smaller packing material sizes (0.18–2 mm in diameter) can lead to either an increase or a decrease of removal efficiency depending on various other conditions and parameters (e.g., gas mixture) [86]. Therefore, the removal efficiency is not only given by a balance between electric field enhancement and gas residence time given by the used packing material size, but it also depends on other parameters as well as on the type of packing material [92].

## 2.4. Analysis of Naphthalene Decomposition By-Products

The evaluation of NRE and EE was supplemented by the analysis of naphthalene decomposition by-products. In principal, an exact composition and yield of by-products were strongly dependent on several parameters, such as applied voltage, discharge power, reactor type, and properties of packing material. The by-products were found in the gas phase as well as in the solid phase as deposits on the reactor walls, inside the gas lines, on windows of the gas cell and surface of packing materials. The two diagnostic methods used for analysis of by-products were scanning electron microscopy (SEM) equipped with energy-dispersive X-ray (EDX) spectroscopy and infrared absorption spectroscopy FTIR. The optical microscope was also used for taking the photographs of packing materials surface.

### 2.4.1. SEM Analysis

A surface analysis of both fresh and used packing materials (i.e., before and after the experiment, respectively) was carried out by means of the SEM. For the analysis, both secondary and backscattered electrons were utilized to obtain surface morphology and to distinguish between areas with different chemical composition, respectively. As electrical resistivity of fresh and used packing materials was quite different, the amplitude of accelerating voltage of scanning electrons for each material was adjusted individually (1.5–20 kV) in order to avoid overcharging of the samples, which could negatively affect an image sharpness. Besides the SEM analysis, we also performed the EDX analysis in order to determine an elemental composition of analyzed surface.

For the fresh packing materials, the SEM analysis allowed us to determine a surface morphology of the pellets, since it consists of pores, granules, and structures of various shapes and sizes. For used packing materials, we identified a shape and a size of solid deposits formed on a surface of the pellets. In addition, we also performed a cross-sectional analysis of used materials after we cut the pellets in half. This allowed us to estimate a thickness of solid deposits accumulated on the surface and also the depth of their penetration inside the pores of packing materials. Table 1 summarizes SEM images and optical microscope images of selected fresh and used materials. Note that various magnifications are used in SEM images, as solid deposits on surface of various packing materials possessed a different size.

**Table 1.** SEM and optical microscope images of fresh, i.e., before experiment (left column), and used, i.e., after the experiment (right column), selected packing materials (magnification in optical microscope images: 160×).

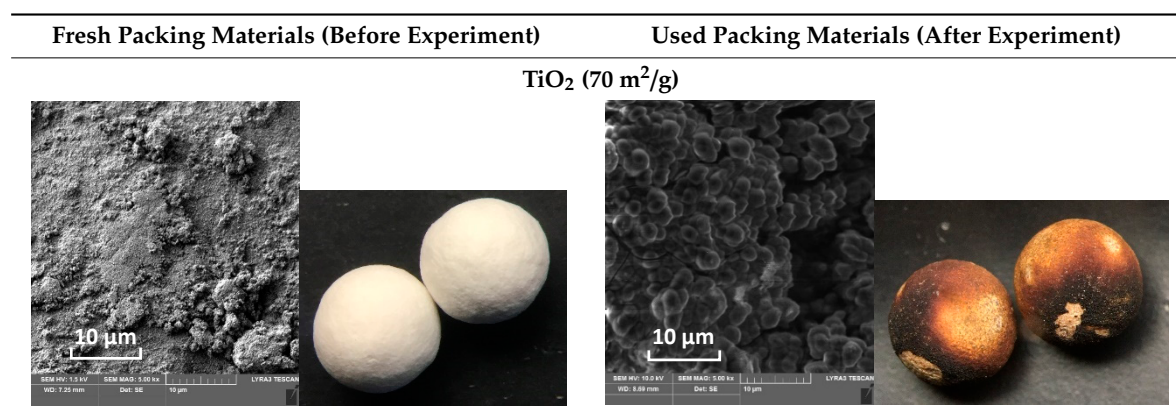
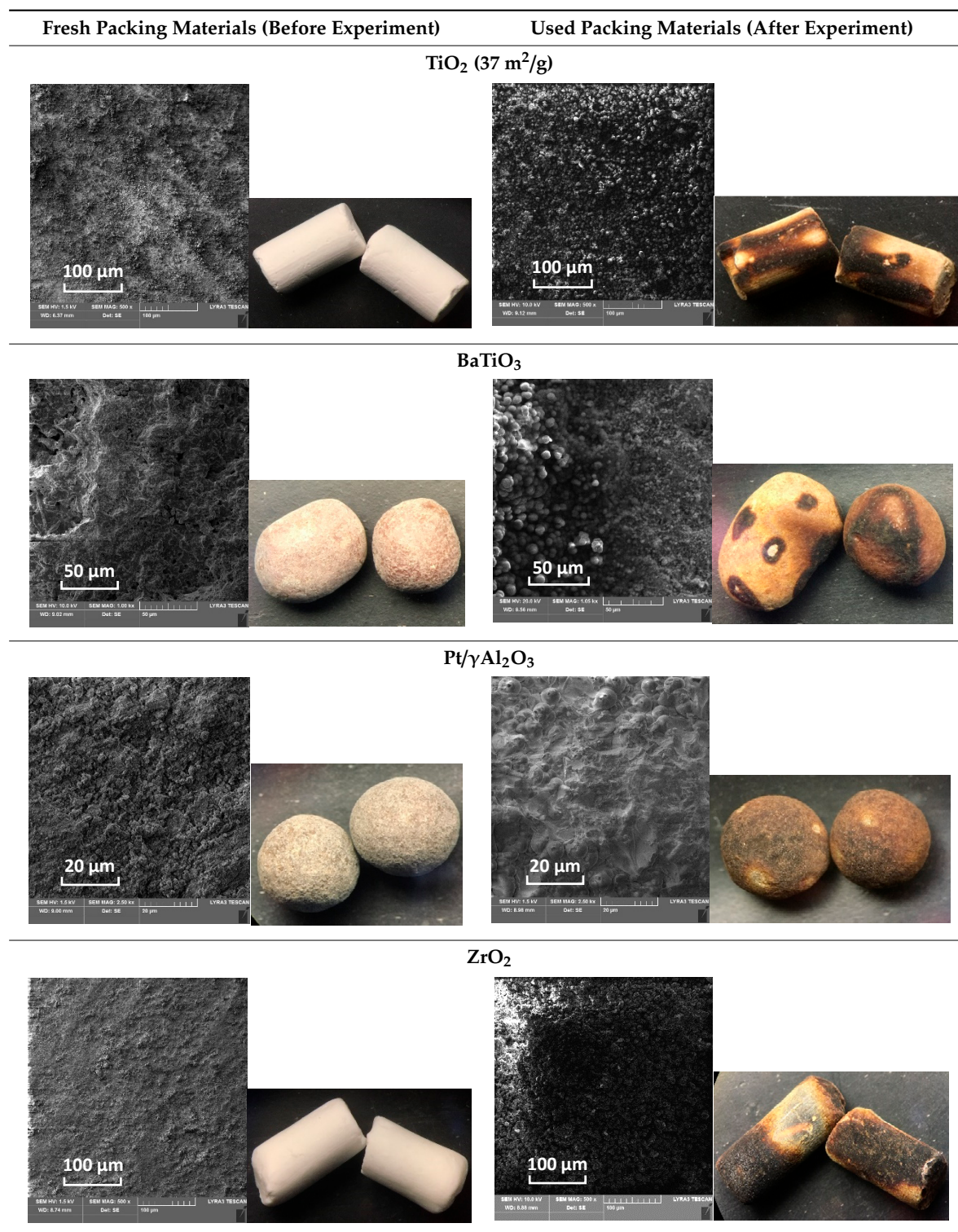


Table 1. Cont.



At first sight, we can see significant differences between photographs of packing materials before and after experiments. The surface of all materials after the experiments acquired a brownish color (Table 1, right column). The change in surface color of materials is attributed to by-products of naphthalene decomposition that formed solid deposits on the surface as a result of the incomplete oxidation of naphthalene. The EDX analysis showed an elemental composition of the deposits and, as was expected, they were mostly composed of carbon and oxygen. The SEM analysis revealed

that the solid deposits were composed of round particles with a diameter in the range of 1–5  $\mu\text{m}$ . These particles also showed strong agglomerating tendencies. A very similar shape of solid carbon deposits resulting from naphthalene decomposition was found by Wang et al.; however, they reported a size of particles of two orders of magnitude smaller than we observed (40–60 nm in diameter) [93]. Such a significant difference in size of carbon particles can be probably explained by different working conditions (temperature of 200  $^{\circ}\text{C}$ ,  $\text{N}_2 + \text{H}_2\text{O}$  as a carrier gas).

Figure 4a shows an SEM image of a cross-sectional view of  $\text{TiO}_2$  surface. Based on this image, it is possible to estimate a thickness of solid carbon deposits (being up to 10  $\mu\text{m}$ ) accumulated on the  $\text{TiO}_2$  surface for 3.5 h of experiment. Figure 4b–f shows detailed SEM images of aggregates of solid deposits on the surface of various packing materials and confirms that round-shape particles of carbon deposits were observed regardless of the packing material type.

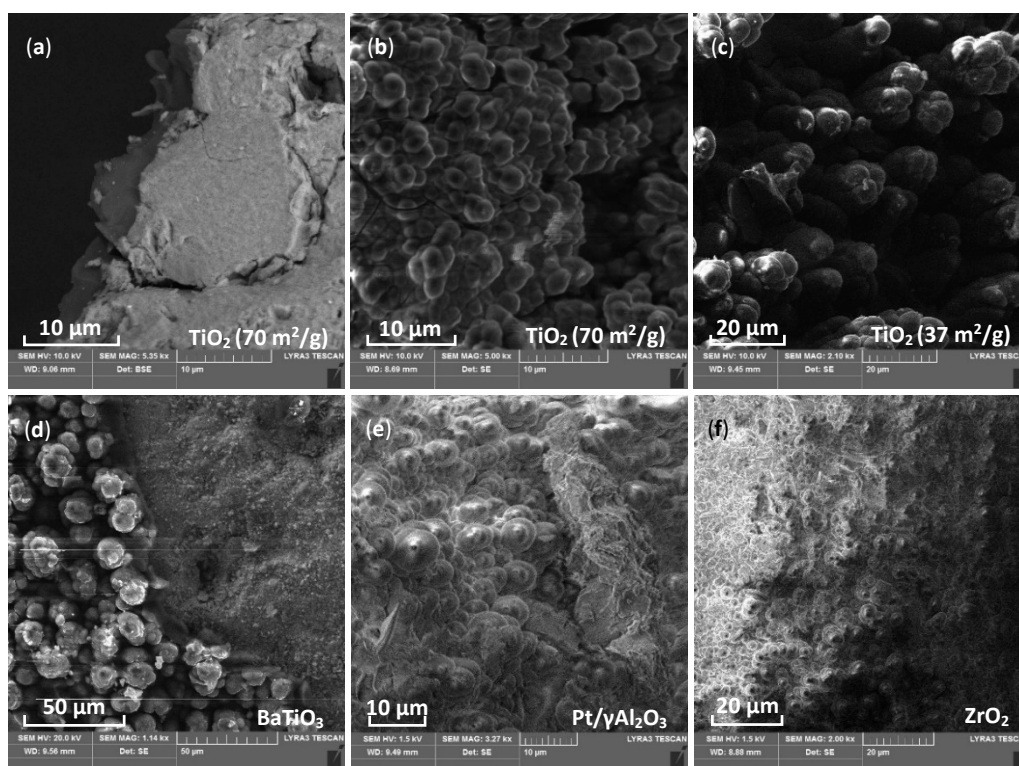


**Figure 4.** Detailed SEM images of (a) cross-sectional view of  $\text{TiO}_2$  surface and (b–f) solid carbon deposits on surface of various packing materials. Note that different magnifications are used.

The packing materials of spherical shape ( $\text{TiO}_2$  of 70  $\text{m}^2/\text{g}$ ,  $\text{Pt}/\gamma\text{Al}_2\text{O}_3$  and  $\gamma\text{Al}_2\text{O}_3$ ) were almost uniformly covered with solid deposits. On the contrary, cylindrical materials ( $\text{TiO}_2$  of 37 and 150  $\text{m}^2/\text{g}$  and  $\text{ZrO}_2$ ) were characterized by nonuniform distribution of deposits (see the images in Table 1). The most specific solid deposits were found on the  $\text{BaTiO}_3$  surface, where they agglomerated in circular patterns with a diameter of approx. 1 mm randomly distributed on the surface (Figure 5a,b). The EDX analysis showed that the circular deposits consisted of carbon and oxygen, while the surrounding was composed of Ba and Ti (Figure 5c,d). The explanation for a formation of such specific circular patterns of deposits can be given as follows: the reactor packed with  $\text{BaTiO}_3$  (i.e., a high dielectric constant material) is governed by filamentary microdischarge mode [52,53,94]. These microdischarges are formed only near the contact points of adjacent pellets where an electric field is extremely strong and where the reactive species are predominantly formed [53]. In the filamentary microdischarge mode, formation of surface discharges propagating along the surface of packing material is completely suppressed, what in turn leads to limited surface area of packing material exposed to generated plasma [6]. Moreover, production of reactive species along the surface of packing material is suppressed

too. Therefore, concentration of reactive species far from the regions of strong electric field significantly decreases. Thus, we hypothesize that naphthalene decomposition process took place only in a close vicinity of filamentary microdischarges (i.e., near the contact points of pellets). Hence, a formation of by-products was also confined in the same regions where a strength of electric field and concentration of reactive species were sufficiently high resulting in circular patterns of solid deposits. Note that most of these circular patterns have a void in their center. We assume that the voids correspond to the places where the adjacent pellets touched each other. Therefore, the solid deposits did not form here.

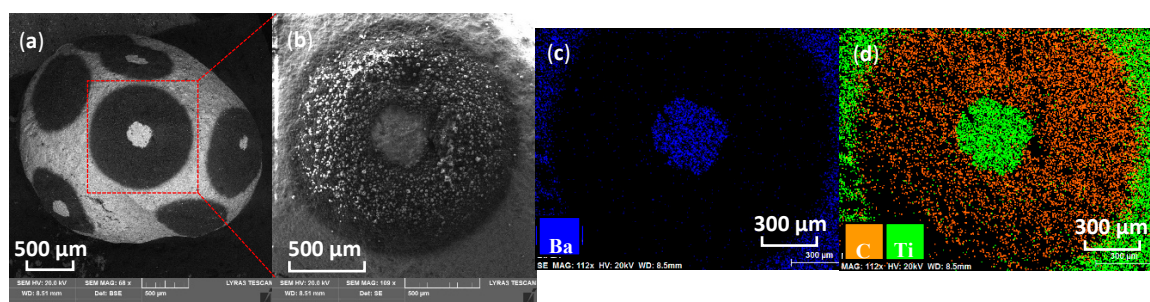


**Figure 5.** (a,b) SEM images and (c,d) EDX analysis of circular patterns of solid deposits on BaTiO<sub>3</sub> surface.

In addition to BaTiO<sub>3</sub>, a few circular patterns of solid deposits were also found on the surfaces of cylindrical pellets (ZrO<sub>2</sub>, TiO<sub>2</sub> of 37 m<sup>2</sup>/g) (Figure 6), whereas on spherical pellets we did not observe them at all. Based on this observation, we further hypothesize that, in the case of spherical pellets of low and moderate dielectric constant, the surface discharges were much more intense than in the case of cylindrical pellets, and resulted in almost uniform distribution of solid by-products along the entire spherical surface. On the other hand, for cylindrical pellets, some circular patterns of solid deposits were found probably as a result of intense filamentary microdischarges rather than surface discharges. This implies that, in addition to a dielectric constant, a packing material shape may also partially affect a discharge mode. The cylindrical pellets have sharper edges that may significantly contribute to local electric field enhancement and, thus, to formation of multiple filamentary microdischarges in contrast to spherical pellets [95]. Thus, the generated plasma is in contact with a limited surface area of packing material, what in turn leads to spatially non-uniform naphthalene decomposition and distribution of by-products along the entire surface (the same, but even stronger effect was observed with BaTiO<sub>3</sub> as mentioned above). Consequently, a confinement of plasma formation to a vicinity of contact points of packing material in contrast to plasma formation and propagation along the surface of packing material (cylindrical vs. spherical pellet, respectively) can possibly explain somewhat counterintuitive results, when the reactor packed with a cylindrical TiO<sub>2</sub> of bigger SSA reached smaller NRE than a spherical TiO<sub>2</sub> of smaller SSA (Figure 3a).

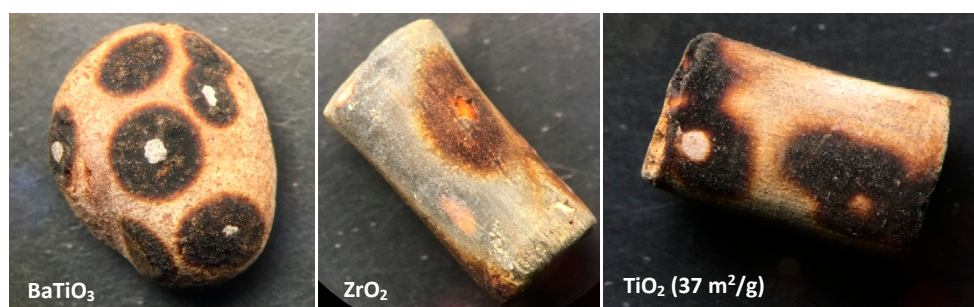


**Figure 6.** Photographs of surface of various packing materials with circular patterns of solid deposits (magnification 250 $\times$ ).

## 2.4.2. FTIR Analysis

The FTIR analysis was conducted for the identification of gaseous and solid by-products of naphthalene decomposition. The gaseous and solid by-products were analyzed individually. Spectra of solid by-products (deposits on windows of the gas cell) were obtained after the experiment when discharge and naphthalene flow were turned off, but solid deposits remained on windows of the gas cell. The spectra of gaseous products were obtained indirectly. Firstly, the combined spectra of gaseous products together with solid by-products were recorded during the experiment. Subsequently, the spectrum of solid by-products was subtracted from the combined spectrum of gaseous and solid by-products to obtain a spectrum of only gaseous products. Thereby, the subtracted spectrum of gaseous products showed narrow absorption bands, while spectra of solid by-products were characterized by intense and very broad bands. Figure 7 shows typical FTIR spectra of gaseous and solid by-products (deposits on the gas cell windows), and the most relevant absorption bands are marked.

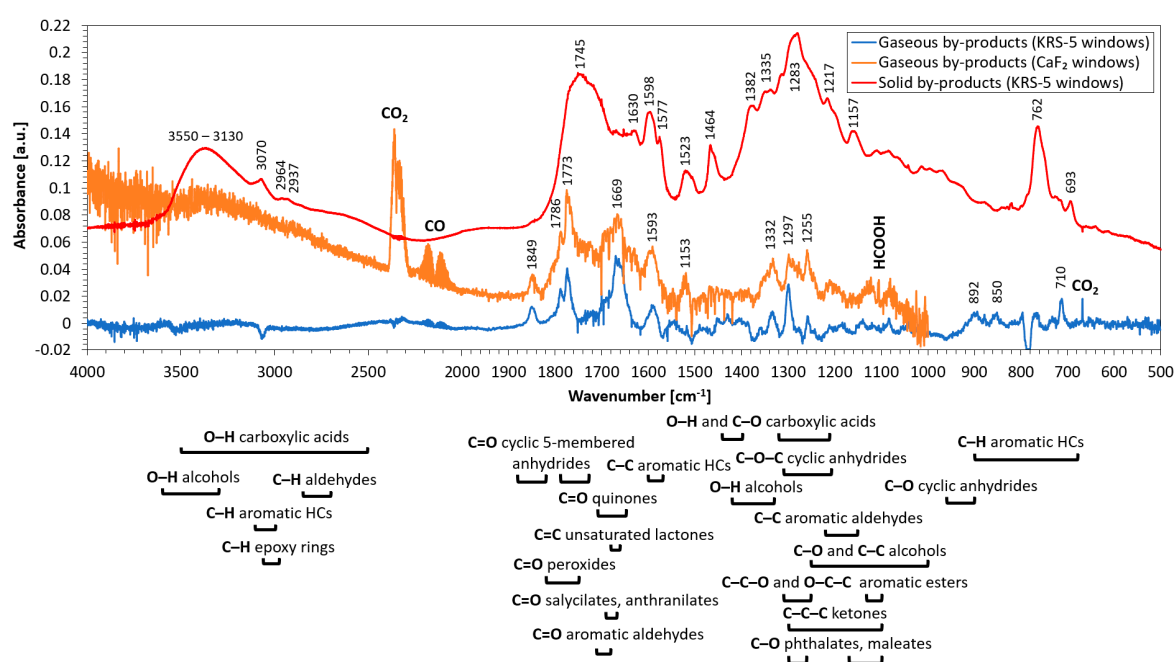


**Figure 7.** Infrared absorption spectra of gaseous (blue and orange line) and solid (red line) by-products of naphthalene decomposition (HCs = hydrocarbons).

The main gaseous products of naphthalene decomposition identified in the FTIR spectra were carbon monoxide CO, carbon dioxide CO<sub>2</sub>, water H<sub>2</sub>O and formic acid HCOOH, along with the nitrous oxide N<sub>2</sub>O and ozone O<sub>3</sub> formed by the reactions in the carrier gas. The concentrations (i.e., production) of two main gaseous products CO and CO<sub>2</sub> depended on reactor type, discharge power and carrier gas. In this work, we used only synthetic air as a carrier gas, while, in our previous work, we also tested the effect of nitrogen and oxygen. In nitrogen, no gaseous products were found, while, in ambient air and oxygen, CO and CO<sub>2</sub> dominated [48]. Among all reactors, the highest CO<sub>2</sub> concentration was obtained with Pt/γAl<sub>2</sub>O<sub>3</sub> (approx. 1140 ppm), while CO concentration was only approx. 180 ppm for 320 J/L. On the contrary, plasma catalytic TiO<sub>2</sub> reactor owned lower CO<sub>2</sub> production (approx. 610 ppm) and higher CO production (approx. 290 ppm) for the same SIE of 320 J/L. It indicates that, although higher NRE was obtained with TiO<sub>2</sub>, more efficient oxidation of naphthalene and formation of gaseous products was observed with Pt/γAl<sub>2</sub>O<sub>3</sub>. In addition to CO and CO<sub>2</sub>, a maximum concentration of HCOOH was found to be approx. 80 ppm. When considering only CO, CO<sub>2</sub>, and HCOOH concentrations, the obtained carbon balance (CB) for all reactors was found to be in a range of 2–4%. More specifically, a plasma non-packed reactor reached CB of approx. 2%, while the reactor packed

with Pt/ $\gamma$ -Al<sub>2</sub>O<sub>3</sub> of approx. 4%. These CB values are indeed very low and significantly underestimated, because other more complex compounds identified among the by-products (discussed below) have not been taken into account, as we identified them only qualitatively and not quantitatively. Low values of CB further imply a low proportion of CO, CO<sub>2</sub>, and HCOOH, and, on the contrary, a very high proportion of other more complex compounds among the by-products. This represents a weakness of our results when compared to the results of other authors. However, an improvement of CB is a scheduled part of our future research.

Besides the main gaseous products of naphthalene decomposition, other more complex gaseous as well as solid compounds were also found in the spectra, although their analysis was not trivial. We reviewed available atlases and databases of FTIR spectra in order to find characteristic organic functional groups and then assigned them to absorption bands in the obtained spectra [96–98]. This approach also allowed for identification of individual compounds in the spectra.

A detailed FTIR spectra analysis of gaseous products revealed that the most intense absorption bands belong to the carbonyl functional group C=O, which is characteristic for a group of compounds including ketones, aldehydes, carboxylic acids, esters, and carbonates. Among the possible compounds, the carboxylic acid anhydrides seem to have the best match with the spectra. As anhydrides contain two carbonyl groups bonded by the same oxygen atom, they show two characteristic C=O absorption bands. The best match was found for cyclic 5-membered carboxylic acid anhydrides that possess unique feature in contrast to straight chain anhydrides: the band at a lower wavenumber is more intense than the band at a higher wavenumber. In general, cyclic anhydrides show two carbonyl bands in the range of 1870–1845 cm<sup>-1</sup> and 1800–1775 cm<sup>-1</sup> (Figure 7) [96]. Out of the anhydrides, the best matches were obtained for phthalic anhydride (1845 and 1775 cm<sup>-1</sup>), maleic anhydride (1848 and 1790 cm<sup>-1</sup>), and naphthalene-1:2-dicarboxylic anhydride (1848–1845 and 1783–1779 cm<sup>-1</sup>) [98].

At lower wavenumbers (1720–1620 cm<sup>-1</sup>), another intense C=O band can be found. The analysis showed a good match with quinones, the group of ketones, which are compounds derived from aromatics by substitution of even number of C–H groups by C=O groups. When two C=O groups are attached to one ring, the quinones absorb in a range of 1690–1660 cm<sup>-1</sup> (Figure 7). Particularly, the 1,2- and 1,4-benzoquinone absorb around 1669 and 1667 cm<sup>-1</sup>, while 1,2- and 1,4-naphthoquinone around 1678 and 1675 cm<sup>-1</sup>, respectively [98].

For cyclic anhydrides, two other absorption bands of C–O and C–C are also relatively intense and can be found at 1300–1180 cm<sup>-1</sup> and 960–880 cm<sup>-1</sup> (Figure 7) [96,99]. In the case of quinones, absorption in a range of 1350–1200 cm<sup>-1</sup> was reported [98]. Furthermore, characteristic bands of aromatic compounds are also present in the spectra. They can be attributed to naphthalene itself or rather to naphthalene-derived compounds. In general, the characteristic C–H absorption bands of aromatic rings occur at 3100–3000 cm<sup>-1</sup> and 900–675 cm<sup>-1</sup>, while C–C bands of medium intensity can be found at 1600–1585 cm<sup>-1</sup> and 1500–1400 cm<sup>-1</sup> (Figure 7) [96,99].

The spectra of solid by-products were analyzed in the same way as gaseous products and several matches for the same compounds were found. However, the analysis was much more complicated due to very broad absorption bands which are typical for solid compounds and also as a result of individual bands overlapping. One of the most striking differences between spectra of gaseous and solid by-products is the presence of very broad band at high wavenumbers in the range of 3600–2700 cm<sup>-1</sup> (Figure 7). The band arises from absorption of hydroxyl O–H group (3500–2500 cm<sup>-1</sup>) usually attributed to alcohols but here more likely to carboxylic acids [96]. In addition, the carboxylic acids also contain bands as follows: C=O (1730–1680 cm<sup>-1</sup>), C–O (1320–1210 cm<sup>-1</sup>) and O–H (1440–1395 cm<sup>-1</sup> and 960–900 cm<sup>-1</sup>) (Figure 7). A good match was also found with salicylic acid (C=O band at 1655 cm<sup>-1</sup>) and benzoic acid (C=O band at 1685 cm<sup>-1</sup>) [98].

Finally, gaseous as well as solid compounds identified in the FTIR spectra based on detailed analysis of functional groups were confronted with the compounds reported as by-products in the works of other authors related to naphthalene decomposition by plasma and plasma catalysis [24,33,35,36,40,44,93,100–104]. The comparison showed a good match and supported our

findings. Thus, we can conclude that, among the complex gaseous products, phthalic anhydride, maleic anhydride, 1,4- and 1,2-naphthoquinone, 1,4-benzoquinone, 1,8-naphthalic anhydride and 3,4-naphthalene-1,2-dicarboxylic anhydride were positively identified. In a solid phase, salicylic acid, phthalide, 1-naphthalenecarboxylic acid, and 1,8-naphthalic anhydride were positively identified. The compounds found in the spectra represent organic gaseous and solid intermediates of naphthalene decomposition and indicate its incomplete oxidation to the desired products of CO<sub>2</sub> and H<sub>2</sub>O.

### 3. Materials and Methods

The experimental setup is depicted in Figure 8. The NTP was generated by atmospheric pressure DBD reactors of cylindrical geometry. The reactors consisted of quartz glass tube (15 mm in diameter, 10 cm in length) and tungsten wire (0.2 mm in diameter) placed in the axis of the tube and aluminum foil wrapped around the tube. The wire served as a high voltage electrode, while the aluminum foil was grounded. The plasma (non-packed) or plasma catalytic (packed) reactors were powered by AC high voltage power supply consisting of a function generator (GwInstek SFG-1013, Taipei, Taiwan), signal amplifier (Omnitronic PAP-350, Waldbüttelbrunn, Germany), and high voltage transformer. The main set of experiments was performed at a frequency of 200 and 500 Hz and for the SIE of 150 and 320 J/L, respectively. Waveforms of the applied voltage and the discharge current were monitored by a high voltage probe (Tektronix P6015A, Berkshire, UK) and current probe (Pearson Electronics 2877, Palo Alto, CA, USA), respectively, both connected to a digital oscilloscope (Tektronix TBS2000, Berkshire, United Kingdom). The power consumption of the reactors was evaluated using the Lissajous figure method with an 82 nF capacitor and a voltage probe (Tektronix P2220, Berkshire, UK). The capacitances of the used reactors were in a range of approx. 1–10 pF.

Synthetic air (purity 5.0) supplied from the pressure tank was used as a carrier gas, and its flow rate was controlled by mass flow controllers (MFC) (Bronkhorst EL-Flow Prestige FG-201CV, Ruurlo, Netherlands). The experimental system including the DBD reactors and gas lines was heated using an electric oven and ribbon heaters to a temperature of 100 °C. Naphthalene (CentralChem, Banská Bystrica, Slovakia) was used as a model tar compound. Two gas lines were used and led to the oven. The air from one line was enriched with naphthalene vapors and then mixed with the air from the second line in order to obtain a desired input naphthalene concentration (approx. 3000 ppm), while total air flow rate was set to 0.5 L/min. The gaseous and solid by-products of naphthalene decomposition were analyzed by means of a Fourier-transform infrared (FTIR) spectrometer (Shimadzu IR-Affinity 1S, Kyoto, Japan) using a gas cell with an optical path length of 10 cm equipped with either CaF<sub>2</sub> or KRS-5 windows. Main gaseous products (CO, CO<sub>2</sub>, and HCOOH) were identified in the FTIR spectra, and their concentrations were evaluated using absorption bands as follows: CO at 2180 cm<sup>-1</sup>, CO<sub>2</sub> at 2360 cm<sup>-1</sup> and HCOOH at 1105 cm<sup>-1</sup>. The solid by-products (deposits) founded on windows of the gas cell were analyzed along with gaseous products. A surface analysis of the fresh and used packing materials was performed by scanning electron microscope (SEM) (Tescan Lyra3, Brno–Kohoutovice, Czech Republic) equipped with an energy-dispersive X-ray spectroscopy (EDX) detector (Bruker 129 eV, Billerica, MA, USA). In addition, the optical stereo microscope (Leica Wild M3C, Wetzlar, Germany) was used for taking the photographs of packing materials surface.

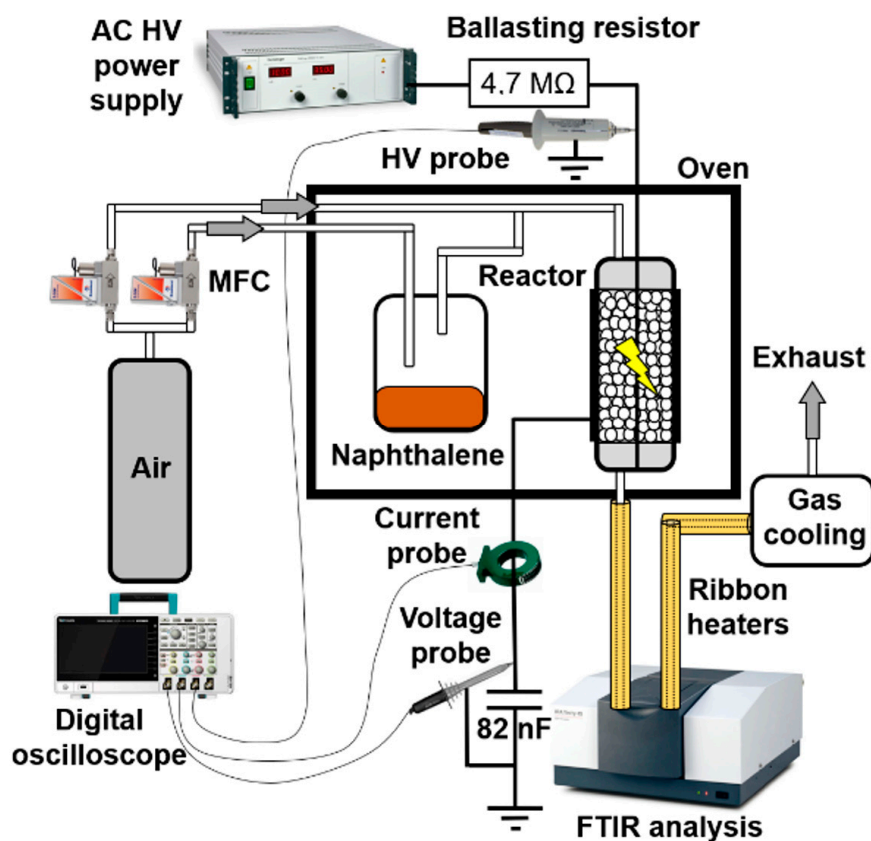


Figure 8. Experimental setup.

The plasma catalytic reactors were filled with various packing materials including catalysts ( $\text{TiO}_2$ ,  $\text{Pt}/\gamma\text{Al}_2\text{O}_3$ ,  $\text{ZrO}_2$ ) and other dielectric materials ( $\text{BaTiO}_3$ ,  $\gamma\text{Al}_2\text{O}_3$ , glass beads). The packing materials were characterized by distinct properties (dielectric constant, shape, size, and specific surface area) summarized in Table 2.

A typical procedure of an individual experiment was comprised of several steps. Firstly, an air with naphthalene vapors was allowed to flow into a reactor and at the same time the discharge was turned on and the SIE was set to 150 J/L. The decomposition of naphthalene induced by the discharge resulted in an increase of CO and  $\text{CO}_2$  concentrations, whereas the naphthalene concentration (evaluated at 781 and  $3067\text{ cm}^{-1}$ ) also gradually increased until it fully stabilized. Once all measured concentrations stabilized, the SIE was increased and set to 320 J/L. Due to an increase of the SIE, naphthalene concentration gradually decreased, and CO and  $\text{CO}_2$  concentrations correspondingly increased as more naphthalene was converted to CO and  $\text{CO}_2$ . When all measured concentrations stabilized again, the discharge was turned off, while air with naphthalene vapors was still allowed to flow into a reactor. The CO and  $\text{CO}_2$  concentrations dropped down to zero, while naphthalene concentration gradually increased until it reached the input concentration. Finally, the naphthalene was turned off and only air was allowed to flow. The experiment was finished once the naphthalene concentration dropped down to zero. The entire experiment typically lasted for 3–7 h. The time depended on the used catalyst and its properties that determined waiting times of the individual steps necessary to reach stabilized concentrations.

**Table 2.** Properties (dielectric constant, shape, size, specific surface area (SSA) and producer) of used packing materials (N/A = not available).

	TiO <sub>2</sub>	BaTiO <sub>3</sub>	Pt/γAl <sub>2</sub> O <sub>3</sub>	γAl <sub>2</sub> O <sub>3</sub>	Glass beads	ZrO <sub>2</sub>
<b>Dielectric constant</b>	20–100 (~85) [52,105]	400–10000 (~4000) [86,106]	~100 [107]	8–11 (~9) [52,85]	~5 [52]	12–25 [19,52,108]
<b>Shape</b>	Spherical, cylindrical	Spherical/cylindrical	Spherical	Spherical	Spherical	Cylindrical
<b>Size [mm] (Ø = diameter; L = length)</b>	Ø 3–4 (sphere) Ø 3–4, L 3–7 (cylinder)	Ø 3–5	Ø 3–4	Ø 3–4	Ø 4, Ø 5	Ø 3, L 4–8
<b>SSA [m<sup>2</sup>/g]</b>	37 (cylinder), 70 (sphere), 150 (cylinder) Sakai Chemicals Co./Abcr GmbH (Osaka, Japan/Karlsruhe, Germany)	N/A	N/A	typically 250–300 [85]	<0.001	90
<b>Producer</b>	Sakai Chemicals Co./Abcr GmbH (Osaka, Japan/Karlsruhe, Germany)	Fuji Titanium Co. (Osaka, Japan)	<i>unknown</i>	Sumitomo Chemical Co. (Tokyo, Japan)	<i>unknown</i>	Abcr GmbH (Karlsruhe, Germany)

The following variables were defined in order to evaluate a performance of DBD reactors:

- *Specific input energy (SIE)* (i.e., energy density or discharge energy per gas volume):

$$\text{SIE (J/L)} = \frac{P}{Q}, \quad (1)$$

where  $P$  and  $Q$  represent power consumption of the discharge and total gas flow rate, respectively.

- *Naphthalene removal efficiency (NRE)*:

$$\text{NRE (\%)} = \left(1 - \frac{c}{c_0}\right) * 100, \quad (2)$$

where  $c_0$  and  $c$  represent the input and output concentrations of naphthalene, respectively.

- *Energy efficiency (EE)* (i.e., the amount of removed naphthalene per specific input energy):

$$\text{EE (g/kWh)} = \frac{\text{NRE} * c_0}{\text{SIE}}, \quad (3)$$

- *Carbon balance (CB)* (i.e., the sum of quantified products per amount of removed carbon):

$$\text{CB (\%)} = \frac{\sum c_{\text{products}}}{n * (c_0 - c)} * 100, \quad (4)$$

where  $\sum c_{\text{products}}$  represents the sum of concentrations of all products, while  $n$  is the number of carbon atoms in molecule of naphthalene (10).

#### 4. Conclusions

In this paper, we investigated the removal of tars by plasma catalysis with naphthalene (C<sub>10</sub>H<sub>8</sub>) as a model tar compound. The NTP was generated by atmospheric pressure DBD reactors and in combination with various packing materials including catalysts (TiO<sub>2</sub>, Pt/γAl<sub>2</sub>O<sub>3</sub>, ZrO<sub>2</sub>) and other dielectric materials (BaTiO<sub>3</sub>, γAl<sub>2</sub>O<sub>3</sub>, glass beads). The packing materials were characterized by a distinct shape (spherical and cylindrical pellets and beads), size (3–5 mm in diameter, 3–8 mm in length),

dielectric constant (5–4000), and specific surface area (SSA) (37–150 m<sup>2</sup>/g). The effects of packing material types and their properties on plasma characteristics, naphthalene removal, and formation of by-products were studied. For the given SIE of 320 J/L, the naphthalene removal efficiency (NRE) of all reactors followed a sequence: TiO<sub>2</sub> (88%) > Pt/γAl<sub>2</sub>O<sub>3</sub> (78%) > ZrO<sub>2</sub> (72%) > γAl<sub>2</sub>O<sub>3</sub> (66%) > glass beads (64%) > BaTiO<sub>3</sub> (51%) > plasma only (41%). An improvement of the NRE was observed with increasing SSA of the catalyst; however, the shape of catalyst pellets was found to be even more important: the NRE obtained with cylindrical TiO<sub>2</sub> with SSA of 37 and 150 m<sup>2</sup>/g were 52 and 70%, respectively, while spherical TiO<sub>2</sub> with moderate SSA of 70 m<sup>2</sup>/g achieved even higher NRE of 88% (for 320 J/L). In addition, improvement of the NRE was also found with smaller glass beads (Ø 4 mm) when compared to larger glass beads (Ø 5 mm) (for 320 J/L, 64 vs. 45%, respectively).

The by-products formed by naphthalene decomposition were found in the gas phase as well as in the solid phase as deposits on the windows of the gas cell, reactor walls, and surface of packing materials. Surface analysis of packing materials was carried out by means of the scanning electron microscopy and revealed significant differences in the distribution of solid deposits on the surface of various materials. While spherical packing materials were covered by solid deposits almost uniformly, the deposits on BaTiO<sub>3</sub> and cylindrical packing materials agglomerated in characteristic circular patterns. We assume it is the result of different discharge modes (surface discharge mode vs. filamentary microdischarge mode) that form depending on the used packing material. The FTIR spectroscopy served for the identification of gaseous and solid by-products of naphthalene decomposition. In addition to main gaseous products (CO, CO<sub>2</sub>, H<sub>2</sub>O and HCOOH), several other complex gaseous and solid by-products were also identified (phthalic anhydride, maleic anhydride, 1,4- and 1,2-naphthoquinone, 1,4-benzoquinone, 1,8-naphthalic anhydride, salicylic acid, phthalide, 1-naphthalenecarboxylic acid).

**Author Contributions:** Conceptualization, investigation, performing the experiments, data processing, writing—original draft preparation, R.C.; performing the experiments, M.C.; SEM analysis, L.S.; supervision, investigation, writing—review and editing, K.H. All authors have read and agreed to the published version of the manuscript.

**Funding:** This research was funded by Slovak Research and Development Agency grant APVV-17-0382, Slovak Grant Agency VEGA 1/0419/18, Comenius University grant UK/222/2020 and foundation of Nadácia Pontis (AXA\_19\_09).

**Conflicts of Interest:** The authors declare no conflict of interest.

## References

1. Mizuno, A. Generation of non-thermal plasma combined with catalysts and their application in environmental technology. *Catal. Today* **2013**, *211*, 2–8. [[CrossRef](#)]
2. Whitehead, J.C. Plasma-catalysis: The known knowns, the known unknowns and the unknown unknowns. *J. Phys. D Appl. Phys.* **2016**, *49*, 243001. [[CrossRef](#)]
3. Carreon, M.L. Plasma catalysis: A brief tutorial. *Plasma Res. Express* **2019**, *1*, 043001. [[CrossRef](#)]
4. Neyts, E.C.; Bogaerts, A. Understanding plasma catalysis through modelling and simulation—A review. *J. Phys. D Appl. Phys.* **2014**, *47*, 224010. [[CrossRef](#)]
5. Neyts, E.C.; Ostrikov, K.; Sunkara, M.K.; Bogaerts, A. Plasma Catalysis: Synergistic Effects at the Nanoscale. *Chem. Rev.* **2015**, *115*, 13408–13446. [[CrossRef](#)] [[PubMed](#)]
6. Bogaerts, A.; Zhang, Q.-Z.; Zhang, Y.-R.; Van Laer, K.; Wang, W. Burning questions of plasma catalysis: Answers by modeling. *Catal. Today* **2019**, *337*, 3–14. [[CrossRef](#)]
7. Kim, H.-H.; Ogata, A.; Futamura, S. Oxygen partial pressure-dependent behavior of various catalysts for the total oxidation of VOCs using cycled system of adsorption and oxygen plasma. *Appl. Catal. B Environ.* **2008**, *79*, 356–367. [[CrossRef](#)]
8. Mei, D.; Zhu, X.; Wu, C.; Ashford, B.; Williams, P.T.; Tu, X. Plasma-photocatalytic conversion of CO<sub>2</sub> at low temperatures: Understanding the synergistic effect of plasma-catalysis. *Appl. Catal. B Environ.* **2016**, *182*, 525–532. [[CrossRef](#)]

9. Tu, X.; Whitehead, J.C. Plasma-catalytic dry reforming of methane in an atmospheric dielectric barrier discharge: Understanding the synergistic effect at low temperature. *Appl. Catal. B Environ.* **2012**, *125*, 439–448. [[CrossRef](#)]
10. Parvulescu, V.I.; Magureanu, M.; Lukes, P. *Plasma Chemistry and Catalysis in Gases and Liquids*; Wiley-VCH Verlag GmbH and Co.: Weinheim, Germany, 2012; ISBN 9783527330065.
11. Pasquiers, S. Removal of pollutants by plasma catalytic processes. *Eur. Phys. J. Appl. Phys.* **2006**, *184*, 177–184. [[CrossRef](#)]
12. Hammer, T.; Kishimoto, T.; Miessner, H.; Rudolph, R. Plasma enhanced selective catalytic reduction: Kinetics of NO<sub>x</sub>-removal and byproduct formation. *SAE Trans.* **1999**, *108*, 2035–2041. [[CrossRef](#)]
13. Liu, M.; Li, J.; Liu, Z.; Zhao, Y.; Jiang, N.; Wu, Y. Improve low-temperature selective catalytic reduction of NO<sub>x</sub> with NH<sub>3</sub> by ozone injection. *Int. J. Plasma Environ. Sci. Technol.* **2020**, *14*, e01007. [[CrossRef](#)]
14. Van Durme, J.; Dewulf, J.; Leys, C.; Van Langenhove, H. Combining non-thermal plasma with heterogeneous catalysis in waste gas treatment: A review. *Appl. Catal. B Environ.* **2008**, *78*, 324–333. [[CrossRef](#)]
15. Vandenbroucke, A.M.; Morent, R.; De Geyter, N.; Leys, C. Non-thermal plasmas for non-catalytic and catalytic VOC abatement. *J. Hazard. Mater.* **2011**, *195*, 30–54. [[CrossRef](#)]
16. Veerapandian, S.K.P.; Leys, C.; De Geyter, N.; Moren, R. Abatement of VOCs using packed bed non-thermal plasma reactors: A review. *Catalysts* **2017**, *7*, 113. [[CrossRef](#)]
17. Whitehead, J.C. Plasma catalysis: A solution for environmental problems. *Pure Appl. Chem.* **2010**, *82*, 1329–1336. [[CrossRef](#)]
18. Liu, L.; Zhang, Z.; Das, S.; Kawi, S. Reforming of tar from biomass gasification in a hybrid catalysis-plasma system: A review. *Appl. Catal. B Environ.* **2019**, *250*, 250–272. [[CrossRef](#)]
19. Michielsen, I.; Uytendhouwen, Y.; Pype, J.; Michielsen, B.; Mertens, J.; Reniers, F.; Meynen, V.; Bogaerts, A. CO<sub>2</sub> dissociation in a packed bed DBD reactor: First steps towards a better understanding of plasma catalysis. *Chem. Eng. J.* **2017**, *326*, 477–488. [[CrossRef](#)]
20. Puliyalil, H.; Lašič Jurković, D.; Dasireddy, V.D.B.C.; Likozar, B. A review of plasma-assisted catalytic conversion of gaseous carbon dioxide and methane into value-added platform chemicals and fuels. *RSC Adv.* **2018**, *8*, 27481–27508. [[CrossRef](#)]
21. Gomez-Rueda, Y.; Helsen, L. The role of plasma in syngas tar cracking. *Biomass Convers. Biorefinery* **2020**, *10*, 857–871. [[CrossRef](#)]
22. Sasujit, K.; Dussadee, N.; Tippayawong, N. Overview of tar reduction in biomass-derived producer gas using non-thermal plasma discharges. *Maejo Int. J. Sci. Technol.* **2019**, *13*, 42–61.
23. Saleem, F.; Harris, J.; Zhang, K.; Harvey, A. Non-thermal plasma as a promising route for the removal of tar from the product gas of biomass gasification—A critical review. *Chem. Eng. J.* **2020**, *382*, 122761. [[CrossRef](#)]
24. Pemen, A.J.M.; Nair, S.A.; Yan, K.; van Heesch, E.J.M.; Ptasinski, K.J.; Drinkenburg, A.A.H. Pulsed corona discharges for tar removal from biomass derived fuel gas. *Plasmas Polym.* **2003**, *8*, 209–224. [[CrossRef](#)]
25. Anis, S.; Zainal, Z.A. Tar reduction in biomass producer gas via mechanical, catalytic and thermal methods: A review. *Renew. Sustain. Energy Rev.* **2011**, *15*, 2355–2377. [[CrossRef](#)]
26. Keyte, I.J.; Albinet, A.; Harrison, R.M. On-road traffic emissions of polycyclic aromatic hydrocarbons and their oxy- and nitro-derivative compounds measured in road tunnel environments. *Sci. Total Environ.* **2016**, *566–567*, 1131–1142. [[CrossRef](#)] [[PubMed](#)]
27. Liu, L.; Wang, Q.; Ahmad, S.; Yang, X.; Ji, M.; Sun, Y. Steam reforming of toluene as model biomass tar to H<sub>2</sub>-rich syngas in a DBD plasma-catalytic system. *J. Energy Inst.* **2018**, *91*, 927–939. [[CrossRef](#)]
28. Liu, S.; Mei, D.; Wang, L.; Tu, X. Steam reforming of toluene as biomass tar model compound in a gliding arc discharge reactor. *Chem. Eng. J.* **2017**, *307*, 793–802. [[CrossRef](#)]
29. Saleem, F.; Zhang, K.; Harvey, A. Plasma-assisted decomposition of a biomass gasification tar analogue into lower hydrocarbons in a synthetic product gas using a dielectric barrier discharge reactor. *Fuel* **2019**, *235*, 1412–1419. [[CrossRef](#)]
30. Sun, J.; Wang, Q.; Wang, W.; Song, Z.; Zhao, X.; Mao, Y.; Ma, C. Novel treatment of a biomass tar model compound via microwave-metal discharges. *Fuel* **2017**, *207*, 121–125. [[CrossRef](#)]
31. Tao, K.; Ohta, N.; Liu, G.; Yoneyama, Y.; Wang, T.; Tsubaki, N. Plasma enhanced catalytic reforming of biomass tar model compound to syngas. *Fuel* **2013**, *104*, 53–57. [[CrossRef](#)]

32. Liu, S.Y.; Mei, D.H.; Nahil, M.A.; Gadkari, S.; Gu, S.; Williams, P.T.; Tu, X. Hybrid plasma-catalytic steam reforming of toluene as a biomass tar model compound over Ni/Al<sub>2</sub>O<sub>3</sub> catalysts. *Fuel Process. Technol.* **2017**, *166*, 269–275. [[CrossRef](#)]
33. Jamróz, P.; Kordylewski, W.; Wnukowski, M. Microwave plasma application in decomposition and steam reforming of model tar compounds. *Fuel Process. Technol.* **2018**, *169*, 1–14. [[CrossRef](#)]
34. Devi, L.; Nair, S.A.; Pemen, A.J.M.; Yan, K.; van Heesch, E.J.M.; Ptasinski, K.J.; Janssen, F.J.J.G. Tar removal from biomass gasification processes. In *Biomass and Bioenergy*; Nova Science Publishers: Hauppauge, NY, USA, 2006; pp. 249–274.
35. Gao, X.; Shen, X.; Wu, Z.; Luo, Z.; Ni, M.; Cen, K. The Mechanism of Naphthalene Decomposition in Corona Radical Shower System by DC Discharge. In *Electrostatic Precipitation*; Springer: Berlin/Heidelberg, Germany, 2008; pp. 713–717.
36. Nair, S.A. *Corona Plasma for Tar Removal*; Technische Universiteit Eindhoven: Eindhoven, The Netherlands, 2004; ISBN 9038626665.
37. Blanquet, E.; Nahil, M.A.; Williams, P.T. Reduction of tars from real biomass gasification by a non-thermal plasma-catalytic system. In Proceedings of the ISPC 2017, Montreal, QC, Canada, 31 July–4 August 2017.
38. Blanquet, E.; Nahil, M.A.; Williams, P.T. Enhanced hydrogen-rich gas production from waste biomass using pyrolysis with non-thermal plasma-catalysis. *Catal. Today* **2019**, *337*, 216–224. [[CrossRef](#)]
39. Hübner, M.; Brandenburg, R.; Neubauer, Y.; Röpcke, J. On the Reduction of Gas-Phase Naphthalene Using Char-Particles in a Packed-Bed Atmospheric Pressure Plasma. *Contrib. Plasma Phys.* **2015**, *55*, 747–752. [[CrossRef](#)]
40. Dors, M.; Kurzyńska, D. Tar Removal by Nanosecond Pulsed Dielectric Barrier Discharge. *Appl. Sci.* **2020**, *10*, 991. [[CrossRef](#)]
41. Liu, L.; Liu, Y.; Song, J.; Ahmad, S.; Liang, J.; Sun, Y. Plasma-enhanced steam reforming of different model tar compounds over Ni-based fusion catalysts. *J. Hazard. Mater.* **2019**, *377*, 24–33. [[CrossRef](#)]
42. Redolfi, M.; Blin-Simiand, N.; Duten, X.; Pasquiers, S.; Hassouni, K. Naphthalene oxidation by different non-thermal electrical discharges at atmospheric pressure. *Plasma Sci. Technol.* **2019**, *21*, 055503. [[CrossRef](#)]
43. Wu, Z.; Zhu, Z.; Hao, X.; Zhou, W.; Han, J.; Tang, X.; Yao, S.; Zhang, X. Enhanced oxidation of naphthalene using plasma activation of TiO<sub>2</sub>/diatomite catalyst. *J. Hazard. Mater.* **2018**, *347*, 48–57. [[CrossRef](#)]
44. Kong, X.; Zhang, H.; Li, X.; Xu, R.; Mubeen, I.; Li, L.; Yan, J. Destruction of toluene, naphthalene and phenanthrene as model tar compounds in a modified rotating gliding arc discharge reactor. *Catalysts* **2019**, *9*, 19. [[CrossRef](#)]
45. Mei, D.; Liu, S.; Wang, Y.; Yang, H.; Bo, Z.; Tu, X. Enhanced reforming of mixed biomass tar model compounds using a hybrid gliding arc plasma catalytic process. *Catal. Today* **2019**, *337*, 225–233. [[CrossRef](#)]
46. Yuan, M.H.; Chang, C.C.; Chang, C.Y.; Lin, Y.Y.; Shie, J.L.; Wu, C.H.; Tseng, J.Y.; Ji, D.R. Radio-frequency-powered atmospheric pressure plasma jet for the destruction of binary mixture of naphthalene and n-butanol with Pt/Al<sub>2</sub>O<sub>3</sub> catalyst. *J. Taiwan Inst. Chem. Eng.* **2014**, *45*, 468–474. [[CrossRef](#)]
47. Sutton, D.; Kelleher, B.; Ross, J.R.H. Review of literature on catalysts for biomass gasification. *Fuel Process. Technol.* **2001**, *73*, 155–173. [[CrossRef](#)]
48. Cimerman, R.; Račková, D.; Hensel, K. Tars removal by non-thermal plasma and plasma catalysis. *J. Phys. D Appl. Phys.* **2018**, *51*, 274003. [[CrossRef](#)]
49. Taheraslani, M.; Gardeniers, H. Coupling of CH<sub>4</sub> to C<sub>2</sub> hydrocarbons in a packed bed DBD plasma reactor: The effect of dielectric constant and porosity of the packing. *Energies* **2020**, *13*, 468. [[CrossRef](#)]
50. Dou, B.; Bin, F.; Wang, C.; Jia, Q.; Li, J. Discharge characteristics and abatement of volatile organic compounds using plasma reactor packed with ceramic Raschig rings. *J. Electrostat.* **2013**, *71*, 939–944. [[CrossRef](#)]
51. Mei, D.; Zhu, X.; He, Y.L.; Yan, J.D.; Tu, X. Plasma-assisted conversion of CO<sub>2</sub> in a dielectric barrier discharge reactor: Understanding the effect of packing materials. *Plasma Sources Sci. Technol.* **2015**, *24*, 15011. [[CrossRef](#)]
52. Van Laer, K.; Bogaerts, A. How bead size and dielectric constant affect the plasma behaviour in a packed bed plasma reactor: A modelling study. *Plasma Sources Sci. Technol.* **2017**, *26*, 085007. [[CrossRef](#)]
53. Wang, W.; Kim, H.H.; Van Laer, K.; Bogaerts, A. Streamer propagation in a packed bed plasma reactor for plasma catalysis applications. *Chem. Eng. J.* **2018**, *334*, 2467–2479. [[CrossRef](#)]
54. Tu, X.; Gallon, H.J.; Twigg, M.V.; Gorry, P.A.; Whitehead, J.C. Dry reforming of methane over a Ni/Al<sub>2</sub>O<sub>3</sub> catalyst in a coaxial dielectric barrier discharge reactor. *J. Phys. D Appl. Phys.* **2011**, *44*, 274007. [[CrossRef](#)]

55. Tu, X.; Gallon, H.J.; Whitehead, J.C. Transition behavior of packed-bed dielectric barrier discharge in argon. *IEEE Trans. Plasma Sci.* **2011**, *39*, 2172–2173. [[CrossRef](#)]
56. Zhang, Q.Z.; Bogaerts, A. Propagation of a plasma streamer in catalyst pores. *Plasma Sources Sci. Technol.* **2018**, *27*, 035009. [[CrossRef](#)]
57. Zhang, Y.-R.; Van Laer, K.; Neyts, E.C.; Bogaerts, A. Can plasma be formed in catalyst pores? A modeling investigation. *Appl. Catal. B Environ.* **2016**, *185*, 56–67. [[CrossRef](#)]
58. Hensel, K.; Martišovítš, V.; Machala, Z.; Janda, M.; Leštinský, M.; Tardiveau, P.; Mizuno, A. Electrical and optical properties of AC microdischarges in porous ceramics. *Plasma Process. Polym.* **2007**, *4*, 682–693. [[CrossRef](#)]
59. Lee, B.Y.; Park, S.H.; Lee, S.C.; Kang, M.; Choung, S.J. Decomposition of benzene by using a discharge plasma-photocatalyst hybrid system. *Catal. Today* **2004**, *93–95*, 769–776. [[CrossRef](#)]
60. Kang, M.; Kim, B.J.; Cho, S.M.; Chung, C.H.; Kim, B.W.; Han, G.Y.; Yoon, K.J. Decomposition of toluene using an atmospheric pressure plasma/TiO<sub>2</sub> catalytic system. *J. Mol. Catal. A Chem.* **2002**, *180*, 125–132. [[CrossRef](#)]
61. Feng, X.; Liu, H.; He, C.; Shen, Z.; Wang, T. Synergistic effects and mechanism of a non-thermal plasma catalysis system in volatile organic compound removal: A review. *Catal. Sci. Technol.* **2018**, *8*, 936–954. [[CrossRef](#)]
62. Wallis, A.E.; Whitehead, J.C.; Zhang, K. Plasma-assisted catalysis for the destruction of CFC-12 in atmospheric pressure gas streams using TiO<sub>2</sub>. *Catal. Lett.* **2007**, *113*, 29–33. [[CrossRef](#)]
63. Theurich, J.; Bahnemann, D.W.; Vogel, R.; Ehamed, F.E.; Alhakimi, G.; Rajab, I. Photocatalytic degradation of naphthalene and anthracene: GC-MS analysis of the degradation pathway. *Res. Chem. Intermed.* **1997**, *23*, 247–274. [[CrossRef](#)]
64. Ndifor, E.N.; Garcia, T.; Taylor, S.H. Naphthalene oxidation over vanadium-modified Pt catalysts supported on  $\gamma$ -Al<sub>2</sub>O<sub>3</sub>. *Catal. Lett.* **2006**, *110*, 125–128. [[CrossRef](#)]
65. Shie, J.L.; Chang, C.Y.; Chen, J.H.; Tsai, W.T.; Chen, Y.H.; Chiou, C.S.; Chang, C.F. Catalytic oxidation of naphthalene using a Pt/Al<sub>2</sub>O<sub>3</sub> catalyst. *Appl. Catal. B Environ.* **2005**, *58*, 289–297. [[CrossRef](#)]
66. Sellick, D.R.; Morgan, D.J.; Taylor, S.H. Silica supported platinum catalysts for total oxidation of the polyaromatic hydrocarbon naphthalene: An investigation of metal loading and calcination temperature. *Catalysts* **2015**, *5*, 690–702. [[CrossRef](#)]
67. Ndifor, E.N.; Carley, A.F.; Taylor, S.H. The role of support on the performance of platinum-based catalysts for the total oxidation of polycyclic aromatic hydrocarbons. *Catal. Today* **2008**, *137*, 362–366. [[CrossRef](#)]
68. Kamal, M.S.; Razzak, S.A.; Hossain, M.M. Catalytic oxidation of volatile organic compounds (VOCs)—A review. *Atmos. Environ.* **2016**, *140*, 117–134. [[CrossRef](#)]
69. Zhang, Z.; Jiang, Z.; Shangguan, W. Low-temperature catalysis for VOCs removal in technology and application: A state-of-the-art review. *Catal. Today* **2016**, *264*, 270–278. [[CrossRef](#)]
70. Kauppi, E.I.; Honkala, K.; Krause, A.O.I.; Kanervo, J.M.; Lefferts, L. ZrO<sub>2</sub> Acting as a Redox Catalyst. *Top. Catal.* **2016**, *59*, 823–832. [[CrossRef](#)]
71. Yamaguchi, T. Application of ZrO<sub>2</sub> as a catalyst and a catalyst support. *Catal. Today* **1994**, *20*, 199–217. [[CrossRef](#)]
72. Rönkkönen, H.; Rikkinen, E.; Linnekoski, J.; Simell, P.; Reinikainen, M.; Krause, O. Effect of gasification gas components on naphthalene decomposition over ZrO<sub>2</sub>. *Catal. Today* **2009**, *147*, 230–236. [[CrossRef](#)]
73. Viinikainen, T.; Rönkkönen, H.; Bradshaw, H.; Stephenson, H.; Airaksinen, S.; Reinikainen, M.; Simell, P.; Krause, O. Acidic and basic surface sites of zirconia-based biomass gasification gas clean-up catalysts. *Appl. Catal. A Gen.* **2009**, *362*, 169–177. [[CrossRef](#)]
74. Juutilainen, S.J.; Simell, P.A.; Krause, A.O.I. Zirconia: Selective oxidation catalyst for removal of tar and ammonia from biomass gasification gas. *Appl. Catal. B Environ.* **2006**, *62*, 86–92. [[CrossRef](#)]
75. Fang, D.; Luo, Z.; Liu, S.; Zeng, T.; Liu, L.; Xu, J.; Bai, Z.; Xu, W. Photoluminescence properties and photocatalytic activities of zirconia nanotube arrays fabricated by anodization. *Opt. Mater.* **2013**, *35*, 1461–1466. [[CrossRef](#)]
76. Fisher, J.; Egerton, T.A. Titanium Compounds, Inorganic. In *Kirk-Othmer Encyclopedia of Chemical Technology*; John Wiley and Sons: Hoboken, NJ, USA, 2001.
77. Machala, Z.; Janda, M.; Hensel, K.; Jedlovský, I.; Leštinská, L.; Foltin, V.; Martišovítš, V.; Morvová, M. Emission spectroscopy of atmospheric pressure plasmas for bio-medical and environmental applications. *J. Mol. Spectrosc.* **2007**, *243*, 194–201. [[CrossRef](#)]

78. Cheng, Z.X.; Zhao, X.G.; Li, J.L.; Zhu, Q.M. Role of support in CO<sub>2</sub> reforming of CH<sub>4</sub> over a Ni/ $\gamma$ -Al<sub>2</sub>O<sub>3</sub> catalyst. *Appl. Catal. A Gen.* **2001**, *205*, 31–36. [[CrossRef](#)]
79. Meephoka, C.; Chaisuk, C.; Samparnpiboon, P.; Praserttham, P. Effect of phase composition between nano  $\gamma$ - and  $\chi$ -Al<sub>2</sub>O<sub>3</sub> on Pt/Al<sub>2</sub>O<sub>3</sub> catalyst in CO oxidation. *Catal. Commun.* **2008**, *9*, 546–550. [[CrossRef](#)]
80. Ogata, A.; Yamanouchi, K.; Mizuno, K.; Kushiyama, S.; Yamamoto, T. Decomposition of benzene using alumina-hybrid and catalyst-hybrid plasma reactors. *IEEE Trans. Ind. Appl.* **1999**, *35*, 1289–1295. [[CrossRef](#)]
81. Sano, T.; Negishi, N.; Sakai, E.; Matsuzawa, S. Contributions of photocatalytic/catalytic activities of TiO<sub>2</sub> and  $\gamma$ -Al<sub>2</sub>O<sub>3</sub> in nonthermal plasma on oxidation of acetaldehyde and CO. *J. Mol. Catal. A Chem.* **2006**, *245*, 235–241. [[CrossRef](#)]
82. Roland, U.; Holzer, F.; Kopinke, F.D. Combination of non-thermal plasma and heterogeneous catalysis for oxidation of volatile organic compounds: Part 2. Ozone decomposition and deactivation of  $\gamma$ -Al<sub>2</sub>O<sub>3</sub>. *Appl. Catal. B Environ.* **2005**, *58*, 217–226. [[CrossRef](#)]
83. Ray, D.; Manoj Kumar Reddy, P.; Subrahmanyam, C. Glass Beads Packed DBD-Plasma Assisted Dry Reforming of Methane. *Top. Catal.* **2017**, *60*, 869–878. [[CrossRef](#)]
84. Holzer, F.; Kopinke, F.D.; Roland, U. Influence of ferroelectric materials and catalysts on the performance of Non-Thermal Plasma (NTP) for the removal of air pollutants. *Plasma Chem. Plasma Process.* **2005**, *25*, 595–611. [[CrossRef](#)]
85. Kim, H.-H.; Teramoto, Y.; Negishi, N.; Ogata, A. A multidisciplinary approach to understand the interactions of nonthermal plasma and catalyst: A review. *Catal. Today* **2015**, *256*, 13–22. [[CrossRef](#)]
86. Butterworth, T.; Elder, R.; Allen, R. Effects of particle size on CO<sub>2</sub> reduction and discharge characteristics in a packed bed plasma reactor. *Chem. Eng. J.* **2016**, *293*, 55–67. [[CrossRef](#)]
87. Xu, S.; Whitehead, J.C.; Martin, P.A. CO<sub>2</sub> conversion in a non-thermal, barium titanate packed bed plasma reactor: The effect of dilution by Ar and N<sub>2</sub>. *Chem. Eng. J.* **2017**, *327*, 764–773. [[CrossRef](#)]
88. Liu, Y.; Li, Z.; Yang, X.; Xing, Y.; Tsai, C.; Yang, Q.; Wang, Z.; Yang, R.T. Performance of mesoporous silicas (MCM-41 and SBA-15) and carbon (CMK-3) in the removal of gas-phase naphthalene: Adsorption capacity, rate and regenerability. *RSC Adv.* **2016**, *6*, 21193–21203. [[CrossRef](#)]
89. Ravenni, G.; Sárossy, Z.; Ahrenfeldt, J.; Henriksen, U.B. Activity of chars and activated carbons for removal and decomposition of tar model compounds—A review. *Renew. Sustain. Energy Rev.* **2018**, *94*, 1044–1056. [[CrossRef](#)]
90. Bogaerts, A.; Kozak, T.; Van Laer, K.; Snoeckx, R. Plasma-based conversion of CO<sub>2</sub>: Current status and future challenges. *Faraday Discuss.* **2015**, *183*, 217–232. [[CrossRef](#)] [[PubMed](#)]
91. Van Laer, K.; Bogaerts, A. Improving the Conversion and Energy Efficiency of Carbon Dioxide Splitting in a Zirconia-Packed Dielectric Barrier Discharge Reactor. *Energy Technol.* **2015**, *3*, 1038–1044. [[CrossRef](#)]
92. Whitehead, J.C. Plasma-catalysis: Is it just a question of scale? *Front. Chem. Sci. Eng.* **2019**, *13*, 264–273. [[CrossRef](#)]
93. Wang, Y.; Yang, H.; Tu, X. Plasma reforming of naphthalene as a tar model compound of biomass gasification. *Energy Convers. Manag.* **2019**, *187*, 593–604. [[CrossRef](#)]
94. Zhang, Q.-Z.; Wang, W.-Z.; Bogaerts, A. Importance of surface charging during plasma streamer propagation in catalyst pores. *Plasma Sources Sci. Technol.* **2018**, *27*, 065009. [[CrossRef](#)]
95. Takaki, K.; Urashima, K.; Chang, J.S. Ferro-electric pellet shape effect on C<sub>2</sub>F<sub>6</sub> removal by a packed-bed-type nonthermal plasma reactor. *IEEE Trans. Plasma Sci.* **2004**, *32*, 2175–2183. [[CrossRef](#)]
96. Smith, B. *Infrared Spectral Interpretation: A Systematic Approach*; CRC Press: Boca Raton, FL, USA, 1999; ISBN 0849324637.
97. Socrates, G. *Infrared and Raman Characteristic Group Frequencies Contents*; John Wiley and Sons: Hoboken, NJ, USA, 2001; ISBN 0471852988.
98. Bellamy, L.J. *The Infrared Spectra of Complex Molecules*; John Wiley and Sons: Hoboken, NJ, USA, 1976; ISBN 9789401160173.
99. Silverstein, R.M.; Webster, F.X.; Kiemle, D.J. *Spectrometric Identification of Organic Compounds*; John Wiley and Sons: Hoboken, NJ, USA, 2005; ISBN 0-471-39362-2.
100. Xu, R.; Zhu, F.; Zhang, H.; Ruya, P.M.; Kong, X.; Li, L.; Li, X. Simultaneous Removal of Toluene, Naphthalene, and Phenol as Tar Surrogates in a Rotating Gliding Arc Discharge Reactor. *Energy Fuels* **2020**, *34*, 2045–2054. [[CrossRef](#)]

101. Zhang, H.; Zhu, F.; Li, X.; Xu, R.; Li, L.; Yan, J.; Tu, X. Steam reforming of toluene and naphthalene as tar surrogate in a gliding arc discharge reactor. *J. Hazard. Mater.* **2019**, *369*, 244–253. [[CrossRef](#)] [[PubMed](#)]
102. Ni, M.J.; Shen, X.; Gao, X.; Wu, Z.L.; Lu, H.; Li, Z.S.; Luo, Z.Y.; Cen, K.F. Naphthalene decomposition in a DC corona radical shower discharge. *J. Zhejiang Univ. Sci. A* **2011**, *12*, 71–77. [[CrossRef](#)]
103. Wu, Z.; Wang, J.; Han, J.; Yao, S.; Xu, S.; Martin, P. Naphthalene Decomposition by Dielectric Barrier Discharges at Atmospheric Pressure. *IEEE Trans. Plasma Sci.* **2016**, *45*, 154–161. [[CrossRef](#)]
104. Abdelaziz, A.A.; Seto, T.; Abdel-Salam, M.; Otani, Y. Influence of N<sub>2</sub>/O<sub>2</sub> mixtures on decomposition of naphthalene in surface dielectric barrier discharge based reactor. *Plasma Chem. Plasma Process.* **2014**, *34*, 1371–1385. [[CrossRef](#)]
105. Wypych, A.; Bobowska, I.; Tracz, M.; Opasinska, A.; Kadlubowski, S.; Krzywania-Kaliszewska, A.; Grobelny, J.; Wojciechowski, P. Dielectric properties and characterisation of titanium dioxide obtained by different chemistry methods. *J. Nanomater.* **2014**, *2014*, 124814. [[CrossRef](#)]
106. Butterworth, T.; Allen, R.W.K. Plasma-catalyst interaction studied in a single pellet DBD reactor: Dielectric constant effect on plasma dynamics. *Plasma Sources Sci. Technol.* **2017**, *26*, 065008. [[CrossRef](#)]
107. Gomaa, M.M.; Gobara, H.M. Electrical properties of Ni/silica gel and Pt/ $\gamma$ -alumina catalysts in relation to metal content in the frequency domain. *Mater. Chem. Phys.* **2009**, *113*, 790–796. [[CrossRef](#)]
108. Harrop, P.J.; Wanklyn, J.N. The dielectric constant of zirconia. *Br. J. Appl. Phys.* **1967**, *18*, 739–742. [[CrossRef](#)]

**Publisher's Note:** MDPI stays neutral with regard to jurisdictional claims in published maps and institutional affiliations.



© 2020 by the authors. Licensee MDPI, Basel, Switzerland. This article is an open access article distributed under the terms and conditions of the Creative Commons Attribution (CC BY) license (<http://creativecommons.org/licenses/by/4.0/>).